Hindawi
Shock and Vibration
Volume 2019, Article ID 5874678, 18 pages
https://doi.org/10.1155/2019/5874678

Research Article

High-Speed Train-Track-Bridge Dynamic Interaction considering Wheel-Rail Contact Nonlinearity due to Wheel Hollow Wear

Chao Chang, Liang Ling, Zhaoling Han, Kaiyun Wang, and Wanming Zhai

State Key Laboratory of Traction Power, Southwest Jiaotong University, Chengdu, Sichuan 610031, China

Correspondence should be addressed to Liang Ling; liangling@swjtu.edu.cn

Received 2 August 2019; Accepted 28 September 2019; Published 31 October 2019

Academic Editor: Sakdirat Kaewunruen

Wheel hollow wear is a common form of wheel-surface damage in high-speed trains, which is of great concern and a potential threat to the service performance and safety of the high-speed railway system. At the same time, rail corridors in high-speed railways are extensively straightened through the addition of bridges. However, only few studies paid attention to the influence of wheel-profile wear on the train-track-bridge dynamic interaction. This paper reports a study of the high-speed train-track-bridge dynamic interactions under new and hollow worn wheel profiles. A nonlinear rigid-flexible coupled model of a Chinese high-speed train travelling on nonballasted tracks supported by a long-span continuous girder bridge is formulated. This modelling is based on the train-track-bridge interaction theory, the wheel-rail nonelliptical multipoint contact theory, and the modified Craig–Bampton modal synthesis method. The effects of wheel-rail nonlinearity caused by the wheel hollow wear are fully considered. The proposed model is applied to predict the vertical and lateral dynamic responses of the high-speed train-track-bridge system under new and worn wheel profiles, in which a high-speed train passing through a long-span continuous girder bridge at a speed of 350 km/h is considered. The numerical results show that the wheel hollow wear changes the geometric parameters of the wheel-rail contact and then deteriorates the train-track-bridge interactions. The worn wheels can increase the vibration response of the high-speed railway bridges.

1. Introduction

Over the last decade, China has constructed the largest high-speed railway network around the world. The mileage of high-speed railway with train running speed from 200 km/h to 350 km/h in China exceeds 29,000 km. Moreover, China plans to construct 38,000 km of passenger dedicated high-speed railway lines by 2025. However, a series of severe challenges including the wear problems of the high-speed wheel/rail systems have to be faced during the operation stage of Chinese high-speed railways. The wear problems of the Chinese high-speed railway include the wheel polygons, rail corrugation, wheel hollow wear, wheel flange wear, rail side wear, and uneven welds, among which the wheel uneven wear is of great concern [1]. With the aggravation of wheel hollow wear, the wheel-rail contact characteristics inevitably change, which then intensifies the high-speed wheel-rail interaction.

Railway corridors in high-speed railways are extensively straightened through the addition of bridges. So, the train-track-bridge dynamic interaction is of great interest in research field of high-speed railways. In fact, the train, the track, and the bridge are an integrated dynamic system, in which the train and the track are coupled by the wheel-rail contact relationship, and the track and the bridge are linked through the track-bridge interaction. As a link connecting the train and the railway infrastructure, the wheel-rail contact relationship plays a crucial role in the high-speed train-track-bridge dynamic interaction. Therefore, the wheel-rail uneven wear not only affects the quality of train operation, but also influences the vibration characteristics of tracks and bridges. Herein, we present a study of the high-speed train-track-bridge dynamic interaction due to the wheel hollow wear, where the wheel-rail contact nonlinearities caused by wheel uneven wear are fully considered.

"Using bridge instead of subgrade" has been widely used in the construction of Chinese high-speed railway. Bridges play a vital role in high-speed railway infrastructure, accounting for more than 50% of total high-speed railway mileage in China, because the use of bridges can avoid the interruption of existing lines and occupy land. With the

increase of speed of passenger trains and because of the fact that taller and longer bridges are being built, the consideration of train-track-bridge interaction becomes more significant [2]. Growing attentions have been paid to the study of train-track-bridge coupled vibration for the last few years [3–10]. For example, Zhai et al. [2] proposed an efficient and practical theoretical model for the analysis of the train-track-bridge interaction, which takes into account a variety of nonlinear factors, aiming to provide a method for analyzing and assessing the running safety and the comfort of high-speed trains passing through bridges [2–4]. Zhang et al. [5, 6] reported a new intersystem iteration method for dynamic analysis of the coupled train-bridge system. In this method, the dynamic responses of train subsystem and bridge subsystem are solved separately, the iteration within time-step is avoided, the computation memory is saved, and it is convenient to use the commercial structural analysis software for bridge subsystem. Li et al. [8] put forward the interactive method by using the commercial finite-element (FE) software ANSYS and multibody dynamics (MBD) software SIMPACK to simulate the vehicle-bridge coupled vibration. It is shown that the interactive method has high computational efficiency and good convergence rate for various bridge, and the vehicle-bridge coupled vibration analysis can be conducted well and followed conveniently by other researchers. Melo et al. [9] developed a numerical vibration prediction scheme for train-bridge systems with FE software ABAQUS and numerical software MATLAB. And the experimental response obtained from a dynamic test under railway traffic revealed a good agreement with the numerical response. Antolín et al. [10] compared four different wheel-rail contact models (nonlinear; linear; rigid; and virtual path) in vehicle-bridge coupling vibration. The numerical investigation found that the forces obtained by non-linear wheel-rail contact model are generally larger than those of other three models, mainly because frictional slip exist in the real wheel-rail contact conditions. Arvidsson et al. [11] established a 2D train-track-bridge interaction model that allows for wheel-rail contact loss to analyze the dynamic performance of high-speed trains running on nonballasted bridges in Europe.

More and more research focus on train-track-bridge safety performance. Dhanasekar et al. [12, 13] studied the impact coefficient and local deformation of long-span suspension bridges and other bridges under actual train loads. Zhang et al. [14] carried out a detailed study on the safety of train operation due to the settlement of high-speed railway bridges, and put forward the corresponding safety limit of pier settlement. Zeng et al. [15–18] applied the actual recorded seismic wave data or pseudo-excitation method (PEM) to analyze the responses of train-track-bridge system under the excitation of seismic waves. Accordingly, some people have studied how to reduce bridge vibration, such as tuned mass damper (TMD) [19, 20], install fluid viscous dampers [21, 22] and magnetorheological damper equipment on bridge structure [23]. Ling et al. [24, 25] predicted the post-derailment behavior of a freight train composed of one locomotive and several wagons on bridge caused by track irregularity based on a coupled finite-element-multibody dynamics (FE-MBD) theory. Rocha et al. [26, 27] assessed the train running safety passing through bridges based on the probability density evolution method. Other studies include train-bridge coupled simulation of a composite structure bridge [28], train-bridge coupled vibration analysis considering environmental wind loads [29, 30], and the interaction between the train-bridge system and the foundation-soil system by the substructure method [31].

Besides, numerous scholars have done a lot of work on the wheel wear and its influence on railway vehicle dynamics. Polach and Nicklisch [32] presented a new standard to identify wheel-rail contact geometry parameters related to vehicle behavior. The new parameter called contact concentration index makes up for the shortcomings of traditional equivalent conicity and assess new proposals for wheel and rail profiles regarding their wear in service. Shi et al. [33] demonstrated the wheel wear evolution and related vehicle dynamics of Chinese high-speed trains with an operating distance of around two million kilometers by a long-term experimental test. Ren [34] proposed a three-dimensional wheel flat model considering the length, width and depth of the flat spot. Thus, it is more in line with the real wheel damage state. The results indicated that the width, the length of the wheel flat, and the width/length ratio have an obvious influence on the wheel/rail impact dynamics.

However, few scholars pay attention to the influence of wheel uneven wear on the dynamic response of high-speed train-track-bridge system. In the traditional studies of train-track-bridge interaction, the wheel and rail profiles were considered as new profiles. This is because the wheel-rail rolling contact algorithms adopted in the traditional train-track-bridge interaction models are difficult to consider the nonlinear contact characteristics of uneven worn wheel and rail profiles. Therefore, a nonlinear rigid-flexible coupled model of high-speed train-track-bridge interaction is formulated. This modelling is based on the train-track-bridge interaction theory, the wheel-rail nonelliptical multipoint contact theory and the modified Craig–Bampton modal synthesis method. The effects of wheel-rail multipoint and conformal contact behaviors caused by the wheel hollow wear are fully considered. The proposed model is then applied to predict the vertical and lateral responses of the high-speed train-track-bridge system under new and worn wheel profiles, in which a high-speed train passing through a long-span continuous girder bridge at speed of 350 km/h is considered. Based on the measured high-speed train worn wheel profiles, the wheel-rail contact geometry of wheel profiles at different mileage was analyzed. The influences of wheel hollow wear on vibration responses of the high-speed train-track-bridge system are reported.

2. Numerical Model

A numerical model of high-speed train-track-bridge nonlinear interaction (see Figure 1) is formulated based on the train-track-bridge dynamic interaction theory [35]. The model consists of four sub models: (1) the train dynamics model, (2) the track dynamics model, (3) the bridge dynamics model, and (4) the contact models for wheel-rail

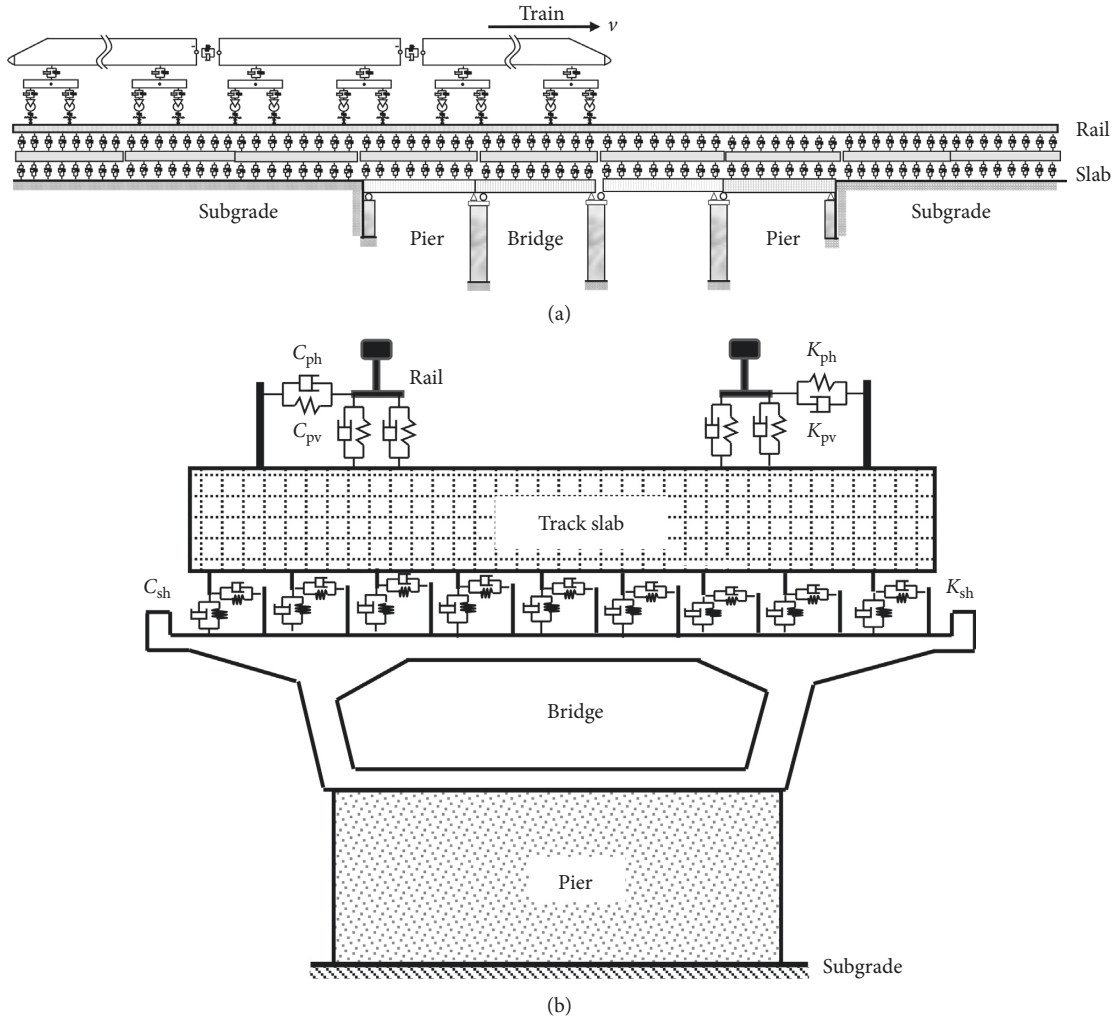

Figure 1: High-speed train-track-bridge coupled dynamic model: (a) side view and (b) end view.

interaction and track-bridge interaction [24]. It fully considers the nonlinear characteristics of the wheel-rail contact, the suspension components of the train, the nonballasted track and complex structure of super-large bridge.

2.1. High-Speed Train Model. A high-speed train fundamentally consists of car bodies, bogies, and wheel sets. The wheel sets are connected with the bogie frame by springs and dampers of the primary suspension system, and the bogie is connected to the car body by a joint through the secondary suspension system including air springs, lateral and vertical dampers, antihunting dampers, and lateral stop. Figure 2 depicts the dimension of wheelbase, bogie center distance, and adjacent wheelbase of CRH2C high-speed train used in this paper.

In this study, a high-speed train consisting of eight vehicles (T + M + M + M + M + M + M + T; M: motor vehicle, T: trailer vehicle) is assumed as a multibody system (MBS), in which the rigid body vibration is categorized into the longitudinal, lateral, vertical, yaw, pitch, and roll motions. For each vehicle model, 15 rigid bodies are considered. Among them, the car body, the bogie frame, and the wheel set each have 6 degrees of freedom (DOFs), and the axle box has one rotational DOF relative to the wheel set. Thus, each vehicle model has a total of 50 DOFs. The degrees of freedom of each vehicle are listed in Table 1. A schematic model of a vehicle is shown in Figure 3. The symbols Z and β represent the DOFs of the vertical and pitch motions of a component; M and I denote the mass and inertia of a rigid body, the subscripts c, t, and w represent successively the car body, bogie frame, and wheel set; v stands for the running speed of the vehicle; K_{sz} and C_{sz} are the vertical stiffness and damping of the secondary suspension, respectively; K_{pz} and C_{pz} are the vertical stiffness and damping of the primary suspension. Y and Ψ denote the DOFs of the lateral and yaw motions of a component; K_{sy} and C_{sy} are the lateral stiffness and damping of the secondary suspension; K_{sx} and C_{sx} are the longitudinal stiffness and damping of the secondary suspension; K_{py} and C_{py} are the lateral stiffness and damping of the primary suspension; K_{px} and C_{px} are the longitudinal stiffness and damping of the primary suspension; Φ denotes the DOF of the roll motion of a component; K_{rx} and K_{my} represent antirolling stiffness and lateral stop stiffness, respectively;

Figure 2: Composition and main dimensions of the considered CRH2C train (unit: cm).

Table 1: Degrees of freedom of the vehicle.

Component	Type of motion					
	Longitudinal	Lateral	Vertical	Roll	Pitch	Yaw
Car body	X_c	Y_c	Z_c	ϕ_c	β_c	Ψ_c
Bogie frame ($i = 1{\sim}2$)	X_{ti}	Y_{ti}	Z_{ti}	ϕ_{ti}	β_{ti}	Ψ_{ti}
Axle box ($i = 1{\sim}8$)	—	—	—	—	β_{ai}	—
Wheel set ($i = 1{\sim}4$)	X_{wi}	Y_{wi}	Z_{wi}	ϕ_{wi}	β_{wi}	Ψ_{wi}

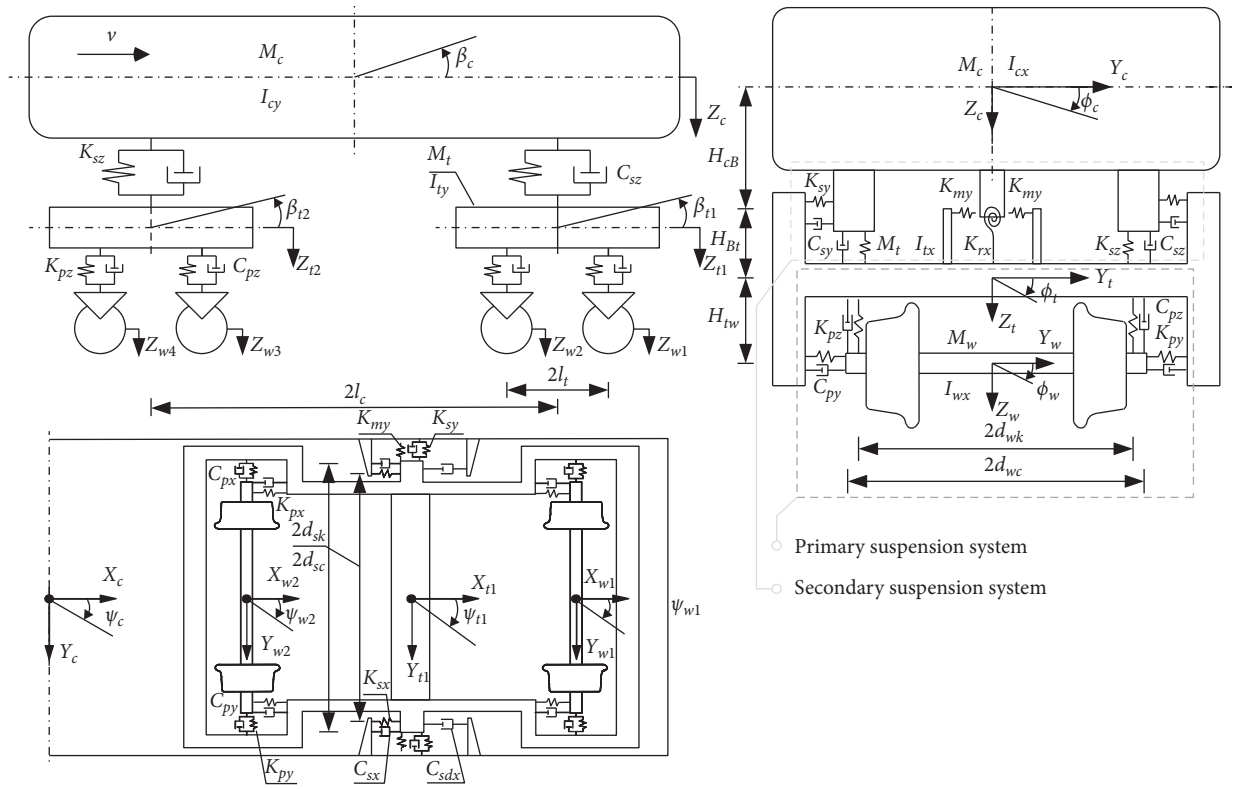

Figure 3: A schematic diagram of the vehicle model.

H_{cb} is the distance from vehicle body center to frame center of mass, and H_{bw} is the distance from frame center of mass to wheel set center of mass.

The train model fully considers the nonlinear elements in the wheel-rail contact geometry relationship, wheel-rail contact forces, and vehicle suspension systems. The damping forces of the vehicle suspension systems are solved by the *Maxwell* models, which consider the stiffness of the joint and the nonlinear behavior of the anti-yaw dampers. The air springs are simulated by the linear spring and damper elements. The rubber bushes and bearings are simulated with special spring and damper elements. The general form of the dynamic equilibrium equations for the train can be expressed as

$$\mathbf{M}_{tv}\ddot{\mathbf{u}}_{tv} + \mathbf{C}_{tv}\dot{\mathbf{u}}_{tv} + \mathbf{K}_{tv}\mathbf{u}_{tv} = \mathbf{f}_{wr}, \tag{1}$$

where $\mathbf{M}_{tv}$ is the mass matrix of the train, $\mathbf{C}_{tv}$ and $\mathbf{K}_{tv}$ are the damping and stiffness matrices, respectively; $\boldsymbol{u}_{tv}$ is the displacement vector of train components; $\mathbf{f}_{wr}$ is the vector of the nonlinear wheel-rail contact forces. The detailed formation of the M, C, and K matrices and their derivation process can be found in [36].

2.2. Track Model. The nonballasted track model consists of rails, slabs, and subgrade, as shown in the lower part of Figure 1. The nonballasted track model consists of two Timoshenko beams for the rails, 3D solid FE model for the

concrete slabs, periodic discrete viscoelastic elements representing the rail fasteners that connect the rails and the slabs, uniformly viscoelastic elements for the cement asphalt layer beneath the slabs. The lateral and vertical bending deformations and torsion of the rails are considered. Each node in the FE track slab model has six DOFs.

The general form of the dynamic equilibrium equations for the track system can be expressed as

$$\mathbf{M}_{tt}\ddot{\mathbf{u}}_{tt} + \mathbf{C}_{tt}\dot{\mathbf{u}}_{tt} + \mathbf{K}_{tt}\mathbf{u}_{tt} = \mathbf{f}_{wr} + \mathbf{f}_{tb}, \tag{2}$$

where $\mathbf{M}_{tt}$ is the mass matrix of the track, $\mathbf{C}_{tt}$ and $\mathbf{K}_{tt}$ are the damping and stiffness matrices, respectively; $\mathbf{u}_{tt}$ is the track displacement vector; $\mathbf{f}_{tb}$ is the vector of the interaction forces with the bridge. The detailed description of the nonballasted track model is given in [3].

2.3. Bridge Model. The bridge structures are modelled with the FE method. The flexible displacements are supposed to be small in the body-fixed frame of reference and could be described in terms of linear FE analysis. Introducing flexible bodies into a model of mechanical system is used for creating the more detailed models and obtaining more accurate results of simulation. As shown in Figure 4, taking the elastic deformation of a simply supported rail bridge as an example, kinematics of bridge is described with the help of the so-called floating frame of reference O_b-$X_bY_bZ_b$. Kinematical formulas are noted in this floating frame of reference. Position of certain point K of the bridge in the global O-XYZ is defined by

$$\mathbf{r}_k = \mathbf{r}_0 + \mathbf{T}_{ob}\mathbf{d}_k = \mathbf{r}_0 + \mathbf{T}_{ob}(\mathbf{u}_b + \boldsymbol{\rho}_k), \tag{3}$$

where $\mathbf{r}_0$ is radius vector of the origin of O_b-$X_bY_bZ_b$ in O-XYZ, $\mathbf{T}_{ob}$ is transformation matrix, $\boldsymbol{\rho}_k$ is radius vector of point K of undistorted flexible body in O_b-$X_bY_bZ_b$, vector $\mathbf{u}_b$ presents elastic displacements of the point.

Small elastic displacements of bridge points in O_b-$X_bY_bZ_b$ are the product of the modal matrix and the matrix-column of modal coordinates

$$\mathbf{u}_b(x,y,z,t) = \begin{bmatrix} u_{bx} \\ u_{by} \\ u_{bz} \end{bmatrix} = \begin{bmatrix} \sum_{i=1}^{S} \phi_{ix}(x,y,z)q_i(t) \\ \sum_{i=1}^{S} \phi_{iy}(x,y,z)q_i(t) \\ \sum_{i=1}^{S} \phi_{iz}(x,y,z)q_i(t) \end{bmatrix} = \sum_{i=1}^{S} \Phi_i q_i = \boldsymbol{\Phi}_b \mathbf{q}_b, \tag{4}$$

where Φ_i is the i-th mode of the bridge, q_i is the modal coordinate that describes flexible displacements correspond to mode i, S is referred as the number of used modes, $\boldsymbol{\Phi}$ is called modal matrix which is solved by the Craig–Bampton modal synthesis method [37].

As shown in Figure 5, the Craig–Bampton fixed interface component mode synthesis method divides the global structure into serval substructures. These substructures are connected with a fixed interface at the interface boundary Γ

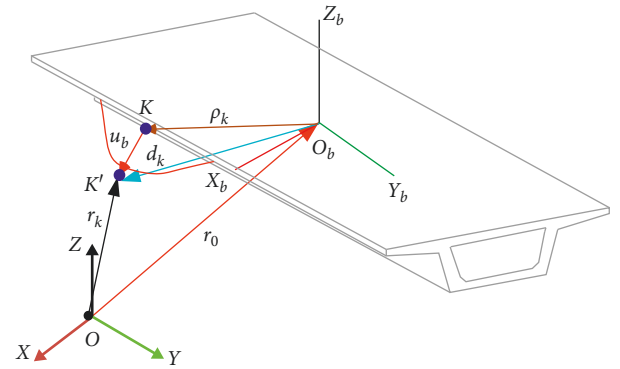

Figure 4: Floating reference frame for the long-span continuous bridge structure.

(Figure 5(c)). Using the Craig–Bampton method, the actual DOFs of bridge are expressed by modal matrix and modal coordinates

$$\mathbf{u}_b = \boldsymbol{\Phi}_b\mathbf{q}_b = \begin{bmatrix} \mathbf{u}_{bB} \\ \mathbf{u}_{bI} \end{bmatrix} = \begin{bmatrix} \mathbf{I}_b & 0 \\ \phi_{IC} & \phi_{IN} \end{bmatrix} \begin{Bmatrix} \mathbf{q}_C \\ \mathbf{q}_N \end{Bmatrix}, \tag{5}$$

in which the subscripts I, B, N, and C in the equation are the indexes to indicate the internal, interfacial, dominant modes, and constrained modes, respectively. ϕ_{IC} is constrained modal set, ϕ_{IC} is dominant modal set (after truncating higher-order modes), $\boldsymbol{u}_{bB}$ and $\boldsymbol{u}_{bI}$ are the interface and internal displacement vectors.

The generalized stiffness matrix and mass matrix in Craig-Bampton method are obtained by modal transformation

$$\begin{aligned} \overline{K}_b &= \boldsymbol{\Phi}_b^T \mathrm{K}_b \boldsymbol{\Phi}_b = \begin{bmatrix} I_b & 0 \\ \phi_{IC} & \phi_{IN} \end{bmatrix}^T \begin{bmatrix} \mathbf{K}_{BB} & \mathbf{K}_{BI} \\ \mathbf{K}_{IB} & \mathbf{K}_{BB} \end{bmatrix} \begin{bmatrix} I_b & 0 \\ \phi_{IC} & \phi_{IN} \end{bmatrix} \\ &= \begin{bmatrix} \overline{K}_{CC} & 0 \\ 0 & \overline{K}_{NN} \end{bmatrix}, \\ \overline{M}_b &= \boldsymbol{\Phi}_b^T \mathbf{M}_b \boldsymbol{\Phi}_b = \begin{bmatrix} I_b & 0 \\ \phi_{IC} & \phi_{IN} \end{bmatrix}^T \begin{bmatrix} \mathbf{M}_{BB} & \mathbf{M}_{BI} \\ \mathbf{M}_{IB} & \mathbf{M}_{BB} \end{bmatrix} \begin{bmatrix} I_b & 0 \\ \phi_{IC} & \phi_{IN} \end{bmatrix} \\ &= \begin{bmatrix} \overline{M}_{CC} & \overline{M}_{NC} \\ \overline{M}_{CN} & \overline{M}_{NN} \end{bmatrix}. \end{aligned} \tag{6}$$

By abstracting the motion of a single elastic body into a linear combination of modal elements (first coordinate transformation), the dynamic equation of the substructure is established, and the dynamic simulation of the elastic body considering the characteristics of the interface is realized. Then the modal coordinates of all substructures are transformed into generalized coordinates (second coordinate transformation) by using the interface connection condition, and the dynamic equation of the system is obtained, and the dynamic characteristics and motion of the whole system are solved. Because there are six rigid body degrees of freedom embedded in the constraint modal set (which must be

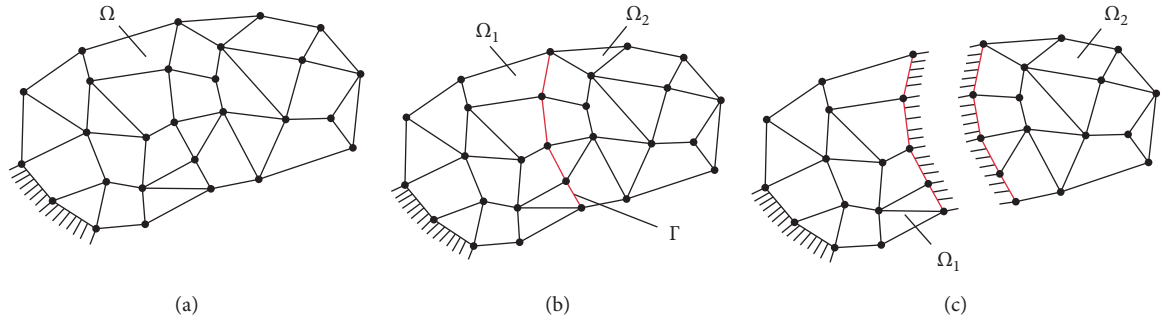

Figure 5: Global and partitioned structural models and interface handling in the Craig–Bampton method. (a) Global (nonpartitioned) structure Ω; (b) substructures Ω_i ($i = 1, 2, \ldots, S$) and interface boundary Γ; (c) interface boundary treatment.

removed before assembly with the multibody system, since the rigid body displacement of components has been defined in the multibody system), and the essence of the constraint modal is static modal. These modes cannot correspond to frequencies, so the Craig–Bampton method needs to be modified so that the elastic substructures can be coupled with the multibody dynamic model and dynamically analyzed [38].

The final step of the preparing set of modes is the orthonormalization of columns of the modal matrix based on eigenvalue problem solution with generalized mass and stiffness matrix. The obtained orthogonal eigenvectors can form transformation matrices N and perform orthogonal transformation.

$$\begin{aligned} \overline{K}_b \mathbf{q}_b &= \overline{\lambda M}_b \mathbf{q}_b, \\ \mathbf{q}_b &= N \overline{q}_b. \end{aligned} \tag{7}$$

The diagonal form of transformed generalized matrices leads to minimal CPU efforts during the integration of equations of motion. It is the basic advantage of such an approach. Another aim of such transformations is the exclusion of modes that correspond to movement of the flexible subsystem as a rigid body. The original modal coordinates are represented by a new Craig–Bampton modal coordinate. So, the physical coordinates can be approximately expressed as

$$\mathbf{u}_b = \sum_{i=1}^{S} \Phi_i q_i = \mathbf{\Phi}_b \mathbf{q}_b \approx \overline{\Phi}_b \overline{q}_b. \tag{8}$$

After assembly and transformation into the global system, the dynamic equilibrium equation for the bridge system can be written as

$$\mathbf{M}_b \ddot{u}_b + \mathbf{C}_b \dot{u}_b + \mathbf{K}_b u_b = \mathbf{f}_{tb}. \tag{9}$$

The bridge damping matrix includes the material damping of the bridge itself and the element damping of the track model can be given by

$$\mathbf{C}_b = \alpha \mathbf{M}_b + \beta \mathbf{K}_b + \sum_{j=1}^{N_e} C_j, \tag{10}$$

where α and β are the Rayleigh damping coefficients; N_e is the number of damping elements; C_j is the damping matrix of the jth track damper element.

$$\begin{cases} \alpha = \dfrac{2\xi_b \omega_i \omega_j}{\omega_i + \omega_j}, \\ \\ \beta = \dfrac{2\xi_b}{\omega_i + \omega_j}, \end{cases} \tag{11}$$

where ω_i and ω_j are the natural frequencies of the two selected flexible modes, ξ_b is the material dependent damping ratio of the bridge, a value of 2% is selected for the concrete bridge.

2.4. Contact Models

2.4.1. Wheel-Rail Contact Model. A wheel-rail nonelliptical multipoint contact model proposed by Kik-Piotrowski [39, 40] is applied to connect the vehicle subsystem and the track subsystem. The Kik-Piotrowski method is a non-Hertzian wheel-rail contact approach based on the virtual penetration theory. It is assumed that the shape of the wheel-rail contact patch can be directly determined by the wheel and rail profiles and the amount of interpenetration. This method can deal with the complex contact situations such as the multipoints and conformal contact conditions caused by wheel-rail profile wear. It is assumed that the normal contact stress p_z is the semielliptical in the rolling direction of the wheel set.

$$p_z(x, y) = \frac{p_0}{x_i(0)} \sqrt{x_i(y)^2 - x^2}, \tag{12}$$

where p_0 is the maximum normal pressure; $x_l(y)$ is the half longitudinal length of the contact patch at the lateral coordinate y. According to the basic assumption of this algorithm, the penetration area is regarded as the contact area. The approximate edges of contact patch consist of intersecting lines of contact surfaces.

$$x_l(y) \cong \sqrt{2Rg(y)}. \tag{13}$$

The normal contact force can be obtained by integrating normal contact stress in the whole contact patch.

$$N = \frac{p_0}{x_l(0)} \int_{y_r}^{y_l} \int_{-x_l(y)}^{x_l(y)} \sqrt{x_l(y)^2 - x^2} \, dx \, dy, \tag{14}$$

where y_l and y_r are the left and right boundary of the wheel-rail contact patch in the y direction, respectively. The normal deformation of the initial contact point (0,0) is

$$w_0 = \frac{1-\mu^2}{\pi E}\frac{p_0}{x_l(0)}\int_{y_r}^{y_l}\int_{-x_l(y)}^{x_l(y)}\sqrt{\frac{x_l(y)^2-x^2}{x^2+y^2}}\,\mathrm{d}x\,\mathrm{d}y. \quad (15)$$

The penetration volume of the contact point is $\delta_0 = 2w(0,0) = 2w_0$, which is based on the above equation.

$$N = \frac{\pi E\delta_0}{2\left(1-\mu^2\right)}\frac{\int_{y_r}^{y_l}\int_{-x_l(y)}^{x_l(y)}\sqrt{x_l(y)^2-x^2}\,\mathrm{d}x\,\mathrm{d}y}{\int_{y_r}^{y_l}\int_{-x_l(y)}^{x_l(y)}\sqrt{\left(x_l(y)^2-x^2\right)/\left(x^2+y^2\right)}\,\mathrm{d}x\,\mathrm{d}y},$$

$$p_0 = \frac{N\sqrt{2R\delta_0}}{\int_{y_r}^{y_l}\int_{-x_l(y)}^{x_l(y)}\sqrt{x_l(y)^2-x^2}\,\mathrm{d}x\,\mathrm{d}y}. \quad (16)$$

After obtaining the clearance and normal contact force of the wheel-rail contact, the calculation of tangential creep forces is carried out based on the FASTSIM algorithm by Kalker [41]. The use of FASTSIM is not only limited to elliptical contact patch but also can obtain good results in multipoint contact conditions.

2.4.2. Track-Bridge Contact Model. For a nonballasted track, the bridge supports the track structure via the cement asphalt layers under the track slabs. In this study, the cement asphalt layers were represented by uniformly distributed nonlinear spring and damper elements (refer to Figure 1(b)). Therefore, the track-bridge contact force $\mathbf{f}_{tb}$ can be calculated by

$$\mathbf{f}_{tb} = \mathbf{K}_{sh}\left(\mathrm{u}_{ts}-\mathrm{u}_b\right)+\mathbf{C}_{sh}\left(\dot{\mathrm{u}}_{ts}-\dot{\mathrm{u}}_b\right). \quad (17)$$

In the above equation, $\mathbf{K}_{sh}$ is the nonlinear stiffness matrix of the cement asphalt layer, $\mathbf{C}_{sh}$ is the nonlinear viscous damping matrix, and $\boldsymbol{u}_{ts}$ is the track slab displacement vector. The detailed derivation process has been given in reference [2].

2.5. Validation of the Model. To verify the accuracy of the proposed train-track-bridge model, the simulation data obtained with the current model is compared with the filed measured data, as shown in Figures 6–8. The field tests were carried out on the Tianjin-Qinhuangdao passenger high-speed railway in China. A total of 13 trains have been measured. The rail displacement and acceleration were measured at the middle span of the 32 m double-track simply supported PC girders with box sections. The trains are reorganized and the speed range is 200–350 km/h. Because the track irregularities of the tested lines were not obtained, the German low-disturbance track spectrum was applied in the simulations. Considering the difference between track irregularity samples used in simulation and the actual track irregularities, the accelerations of axle box and bogie frame are processed by low-pass filtering, and the cut-off frequency is 300 Hz. From the comparison of simulation and test results of the bogie frame acceleration and axle box

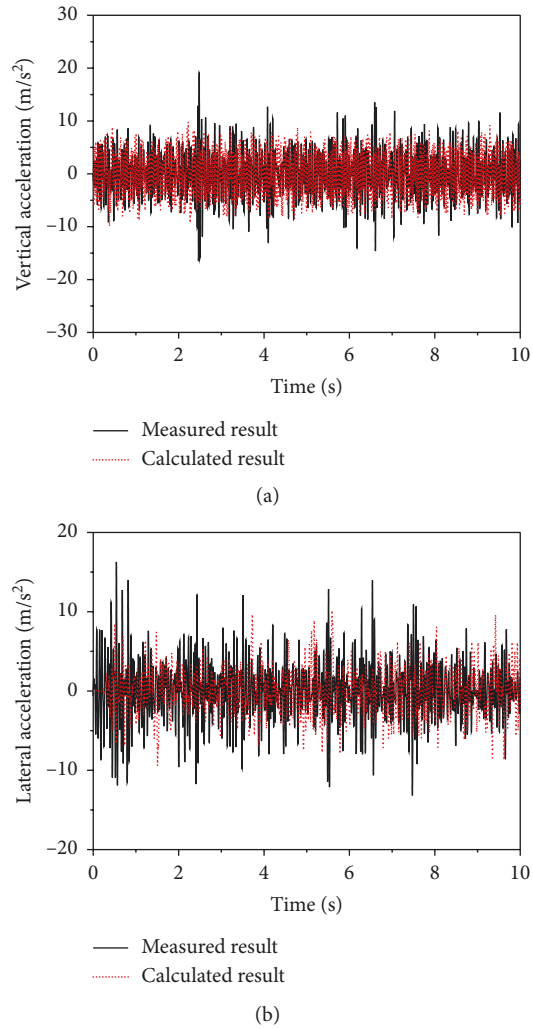

Figure 6: Comparison of measured and calculated result of bogie frame acceleration at a train speed of 350 km/h: (a) time history of vertical acceleration; (b) lateral acceleration.

acceleration (Figures 6 and 7), the simulation results are in good agreement with the test results. Figure 8 is the comparison of the measured and calculated displacement and acceleration of the rails. The simulation results are close to the measured data. Overall, the errors between the results obtained by field test and simulation are negligible, and hence the proposed model can be reliable and reasonable.

3. Variation of Wheel-Rail Contact Geometry due to Wheel Hollow Wear

3.1. Evolution of the Hollow Wear. The evolution of wheel profiles of a Chinese high-speed train is first investigated based on the data from a long-term tracking tests concentrating on the natural wear process of high-speed train wheels [42]. Figure 9 compares several typical worn wheel profiles with different travelling distances. From the changes of the profiles at the nominal rolling circle radius, it can be clearly observed that the wheel hollow wear depth gradually increases with an increase in train operating mileage. The

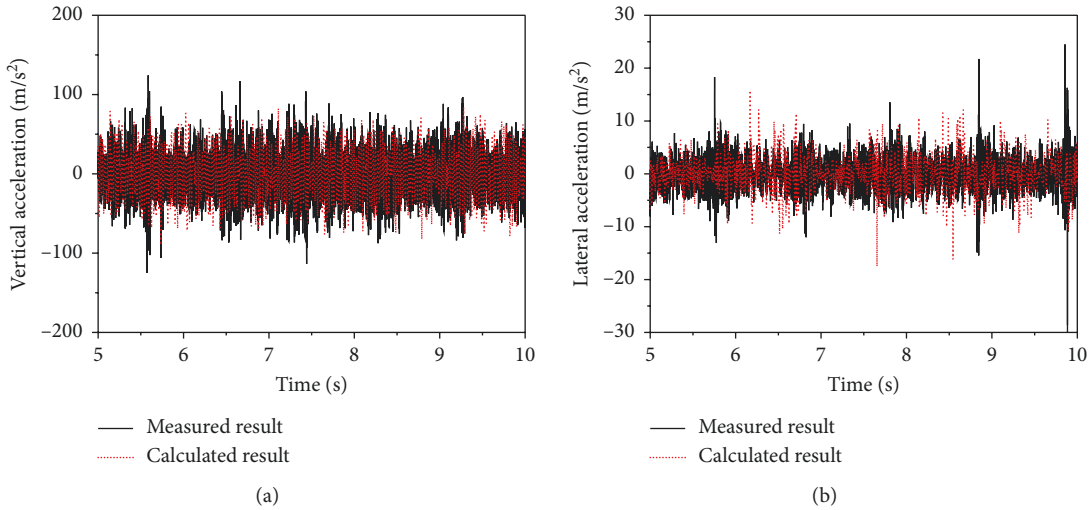

Figure 7: Comparison of measured and calculated result of axle box acceleration at a speed of 350 km/h: (a) time history of vertical acceleration; (b) lateral acceleration.

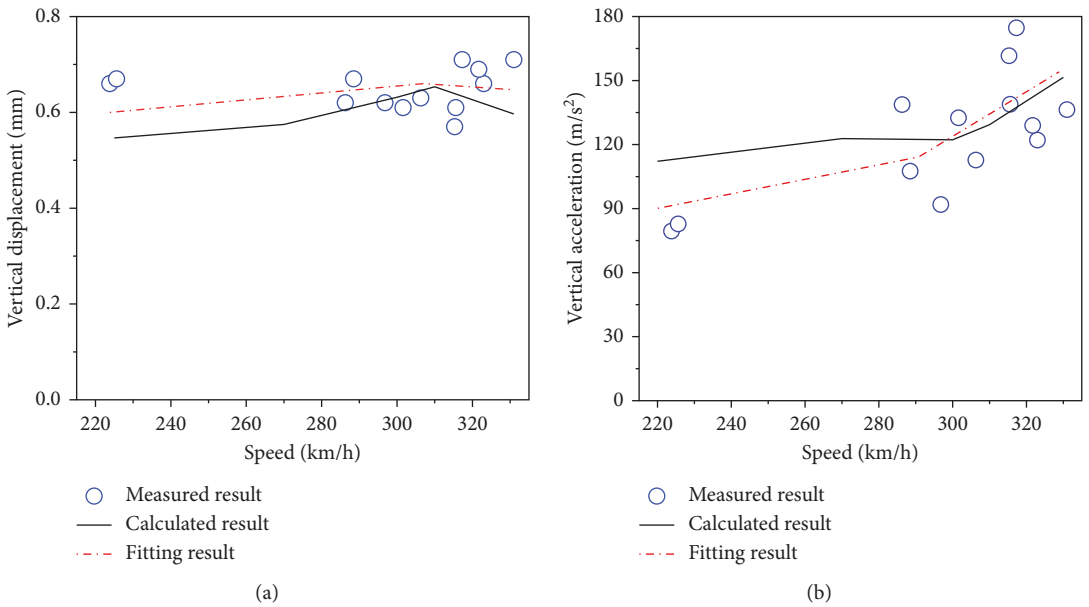

Figure 8: Comparison of measured and calculated result of rail displacement and acceleration: (a) vertical displacement; (b) vertical acceleration.

section of the worn wheel tread around nominal rolling circle is consistent with the new wheel tread.

Figure 10 shows the wear distribution along the wheel width for different travelling distances. It indicates that the main wear region on the wheel tread concentrates on the area ranging from −20 to 20 mm around the nominal rolling circle, and the wear in the flange area is relatively light. This region is the main contact region between the wheel and the rail. With the train travelling distance increase, the wheel wear depth in this region aggravates gradually. According to the field measurement results, the maximum wheel wear depth of the train with travelling distances of 83,000 km, 132,000 km, 169,000 km, and 192,000 km attain 0.34 mm, 0.52 mm, 0.64 mm, and 0.72 mm, respectively, as shown in Figure 10. The region of the worn wheel profiles near the nominal rolling circle presents an obvious concave shape, which substantially affects the wheel-rail contact geometry. The location of the maximum wheel hollow wear depth appears at about +3 mm from the nominal rolling circle radius of the wheel profile.

It should be noted that the wheel hollow wear has reached the limit regulated by *Railway Electric Multiple Units Operation and Maintaining Regulation* [43] after travelling about 210,000 km, and the wheel tread of the tested high-speed train is required to be reprofiled at that time.

3.2. Variation of Wheel-Rail Contact Geometry. The wheel-rail contact geometric analysis for the measured wheel worn

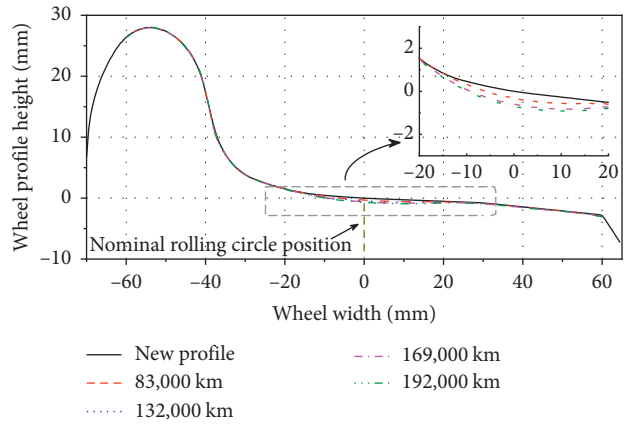

Figure 9: Comparison of measured wheel profiles with different travelling distances.

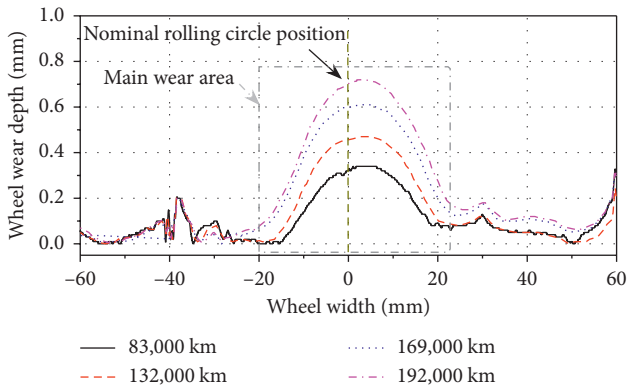

Figure 10: Comparison of measured wheel hollow wear depth for different travelling distances.

and new profiles were carried out respectively. The new CHN60 profile was applied in these analyses. Figure 11 shows the location and layout of contact points of new and worn wheel profiles under different travel mileage. In actual operation of high-speed trains, the wheel set lateral displacement is generally within the range of 10 mm, so the lateral displacement in Figure 11 was set at −10~10 mm.

It is easy to see that the distribution of wheel-rail contact points is concentrated when the new wheel profile matches with the new CHN60 profile. In this case, the distribution of wheel-rail contact points near the wheel flange side is sparse and uniform, which is an ideal one-point contact situation. But when the wheel travel distance is increased to 83,000 km, the wheel-rail contact status evolved from the one-point contact to the multipoint contact, and the distribution of wheel-rail contact points appears in a larger area. The worn wheel-rail contact situations of the wheel travel distance increased to 132,000 and 169,000 km are similar to that of 83,000 km. Compared with the new wheel-rail contact situation, the worn wheel-rail contact points are more dispersed and nonuniform. The contact points at the wheel flange area increase, which also slightly shift to the inside corner of the rails. When the wheel travel distance is increased to 192,000 km, the worn wheel-rail system has an obvious two-point contact trend. Two concentrated wheel-rail contact point areas appear in the center and inside corner of the rails. This means the wheel hollow wear greatly changes the wheel-rail contact status, resulting in a very dispersed and nonuniform distribution of wheel-rail contact points. Under such a severe condition, the wheel-rail two-point contact behavior will occurr frequently. It should be noted that the wheel-rail two-point contact or multipoint contact behavior will intensify wheel-rail interaction and then increase the wear and damage of wheel and rail profiles.

The rolling radius difference, equivalent conicity, contact angle, and contact angle parameters are other four important wheel-rail rolling contact geometric parameters. It can be seen from Figure 12(a) that when the new wheel-rail profile is matched, the rolling radius difference increases slowly with wheel set lateral displacement less than 7 mm. When the wheel set displacement is greater than 7 mm, the rolling radius difference increases sharply. At this time, the wheel-rail contact point approaches the wheel flange, and the curve of rolling circle radius difference presents a nonlinear change law. But for the worn wheels, the fluctuation of rolling radius difference increases obviously when the lateral wheel set displacement is in the range of 1–9 mm. The variation tendency of the rolling radius difference of the wheels with travel distances of 83,000 and 169,000 km are similar, and the fluctuation of the case with travel distances of 192,000 km is the most intense.

For the new profile, the equivalent conicity Figure 12(b)) keeps within 0.1 and changes smoothly when the wheel set displacement is less than 8 mm. But the equivalent conicity of the worn wheel profiles are obviously larger than that of the new profile when the wheel set displacement is larger than 1 mm. The equivalent conicity of the worn wheel profile with travel distances of 192,000 km is larger than that of other cases when the wheel set displacement is in the range of 1–9 mm. The equivalent conicity with a wheel set displacement of 1.5 mm is equal to 0.28. According to the *Klingel* principle, when lateral span and rolling radius of a wheel set are kept constant, an increasing equivalent conicity will increase the bogie hunting motion frequency, and finally decrease the vehicle running stability.

The variation of contact angle and contact angle parameter are shown in Figures 12(c) and 12(d). The contact angle parameter ε is used for linear approximation of the function $E(y)$ on the interval of the lateral shift of the wheel set.

$$E(y) = \frac{\beta_l(y) - \beta_l(y)}{2} \frac{S}{2} \approx \varepsilon y. \tag{18}$$

The designation $\beta_l(y)$, $\beta_r(y)$ are introduced for the contact angles of the left and right wheels depending on the wheel set shift. If the left and right pairs of profiles are equal, the value $\beta_l(0) = \beta_r(0) = \beta_0$ corresponds to the contact angle for symmetric position of the wheel set. The dependence on the lateral shift is used for definition of the contact angle parameter. Here S is the distance between the wheel set rolling radius.

Figure 12 shows that the change of contact angle is gentle for the new wheels when the lateral displacement is in the range of −7–8 mm. But for the worn wheels, the fluctuation

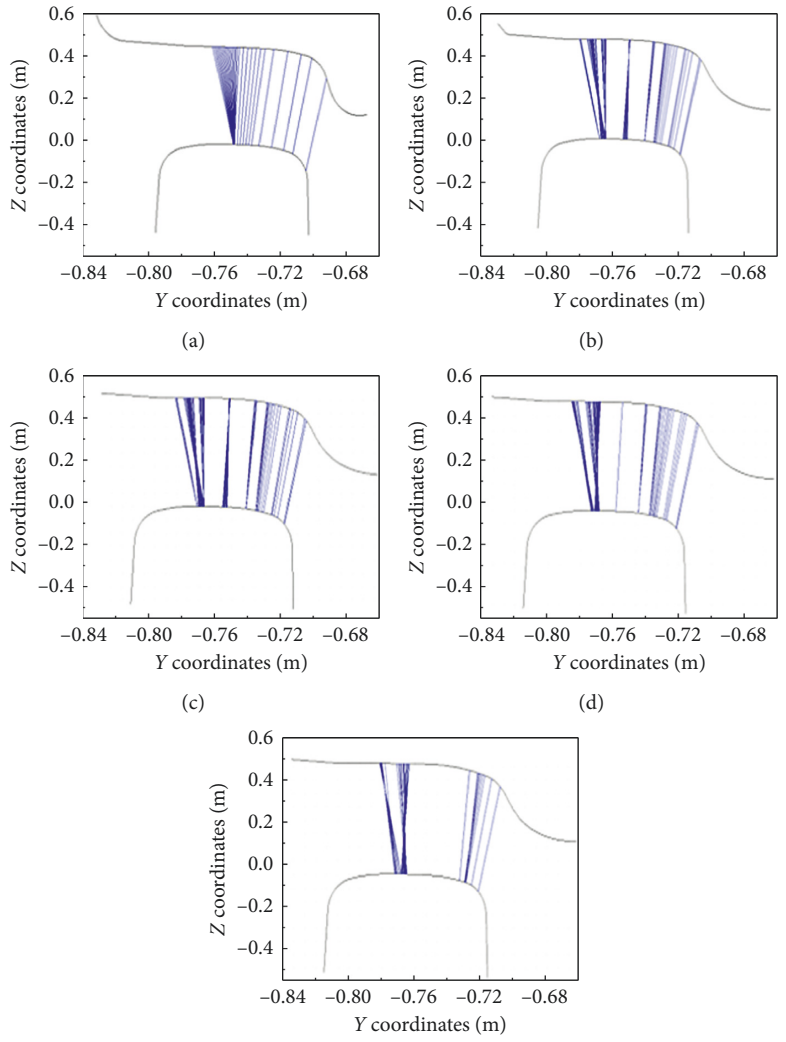

Figure 11: Distribution of wheel-rail contact points of new and worn profiles: (a) new profile; (b) 83,0000 km; (c)132,000 km; (d) 169,000 km; (e) 192,000 km.

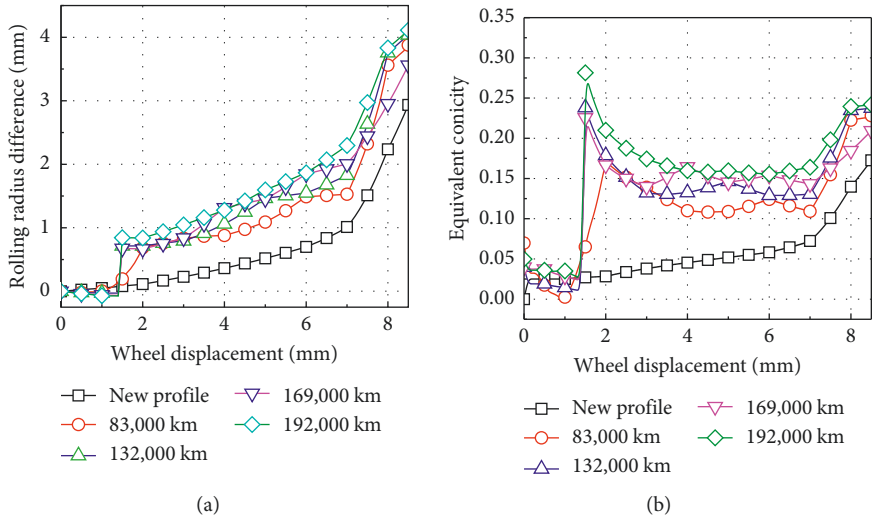

Figure 12: Continued.

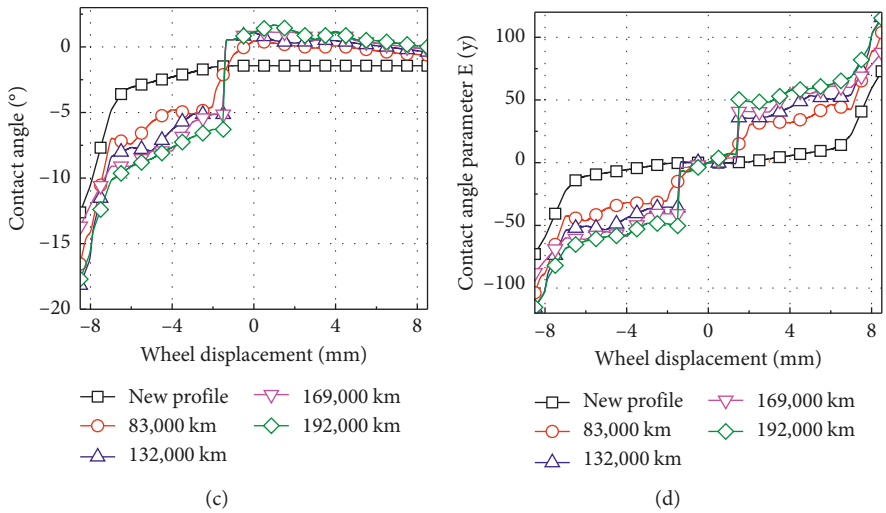

Figure 12: Wheel-rail rolling contact parameters: (a) Rolling circle radius difference; (b) equivalent conicity; (c) contact angle; (d) contact angle parameters.

range of contact angle becomes larger, and there are many sudden changes when the lateral wheel set displacement is negative. With the increasing train travel mileage, the contact characteristics between wheel and rail deteriorate, which led to the increase in the wheel-rail contact angle. The variation trend of wheel-rail contact angle parameters is similar to that of the contact angle.

The above results show that the wheel hollow wear has a great influence on the geometric parameters of the wheel-rail contact, which can aggravate the wheel-rail interaction and finally affect the train-track-bridge interactions.

4. Results and Discussions

The proposed model shown in Section 2 was applied to predict the vertical and lateral responses of the high-speed train-track-bridge system under new and worn wheel profiles, in which a Chinese high-speed train passing through a long-span continuous girder bridge (see Figure 13) at the speed of 350 km/h was considered. Based on the measured high-speed train worn wheel profiles shown in Section 3 and numerical simulations, the influences of wheel hollow wear on vibration responses of the high-speed train-track-bridge system are discussed.

4.1. Illustration of the Bridge. The Chengjiang bridge located in Hechi City of China was selected as example. It is a super-large continuous concrete girder bridge on the Nanning-Guizhou high-speed railway, in which the bridge span is (91.5 + 180 + 91.5) m and the approach bridge is a 24-m prestressed concrete simply supported bridge. A double-track railway is positioned on the bridge and the transverse distance between the railway lines is 5.0 m. The bridge body is mainly made of C55 concrete, and the arch ribs are made of composite materials and steel cables. The overall size of the bridge is shown in Figure 13. The second span box girder of the bridge contains transverse webs, which can enhance the stiffness of the whole bridge structure. The cross section and the main dimensions of the girder are shown in Figure 14.

4.2. FE Model of the Chengjiang Bridge. In the FE modelling of the Chengjiang bridge, several types of elements were applied to simulate the distinct parts of the bridge. Specifically, 3D two-node Euler–Bernoulli beam elements (BEAM188) were used to simulate the arch ribs, transverse structures and diagonal structures based on the actual shape and geometric dimensions of the cross-section properties. Two-node uniaxial link (LINKl0) elements were used to model the bridge cables with three translational DOFs (per node, x, y, and z). Elastic four-node axisymmetric quadrilateral shell elements (SHELL63) with both membrane and bending capabilities were used to simulate the bridge web, deck, and other structures. Shell element is not suitable for the middle and two ends because of their large thickness. So solid element (SOLID185) is used to simulate these parts. Connection between different types of cells is accomplished by coupling nodes with CERIG method, which can eliminate the calculation error caused by different types of elements DOFs inconsistency.

According to the constraints prescribed in the bridge bearing arrangement (see Figure 15), the girder body and pier are connected by the node coupled method. The arrow represents the release direction of the DOFs, whereas the DOF in the arrow direction is not constrained. For example, a single "○" represents that both horizontal and vertical DOFs are constrained and fixed. The overall layout of the bridge FE model is shown in Figure 16. The model consists of 98118 elements and 99938 nodes, which meets the requirement of calculation accuracy through the numerical tests. The two ends of the bridge were connected to the 24 m-length simple supported beam bridges. Three-span simple supported beam bridges were arranged on each side, which can be simulated as conventional beam elements and coupled with the nodes at

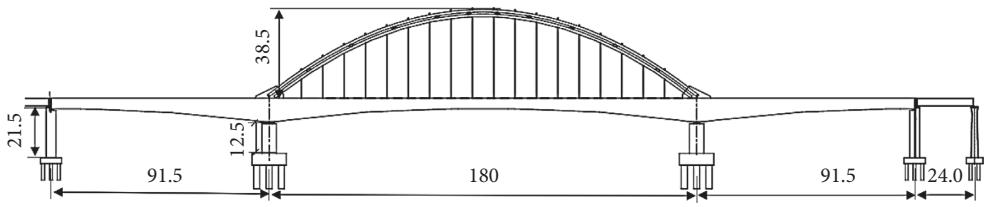

Figure 13: The overall size of the Chengjiang bridge (unit: m).

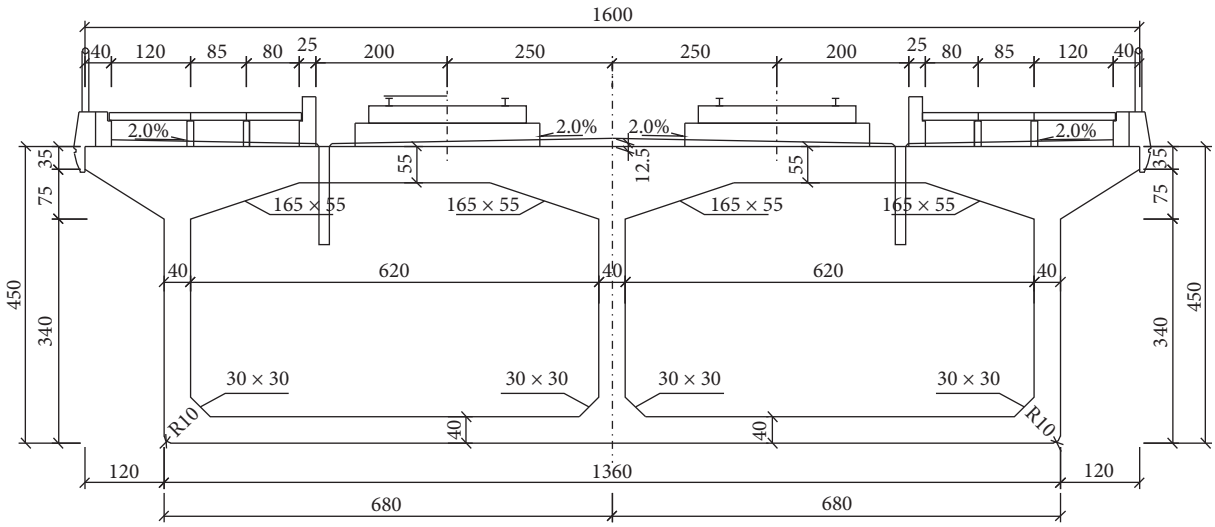

Figure 14: Cross-section of the Chengjiang bridge (unit: cm).

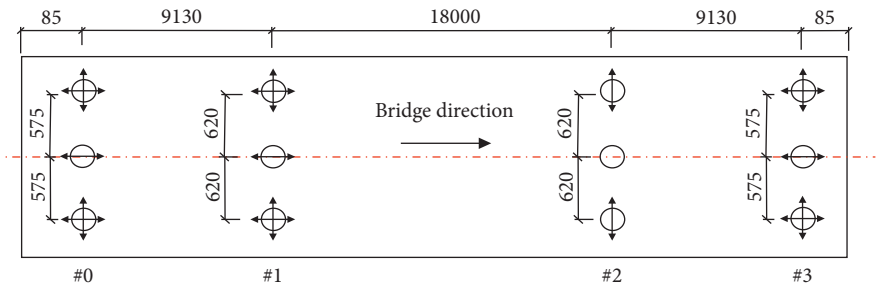

Figure 15: Bridge bearing layout (unit: cm).

both ends of Chengjiang bridge. The bridge FE model was imported into train-track-bridge dynamic interaction calculation program by Craig-Bampton method.

4.3. Results, Discussion, and Comparisons. Based on the proposed high-speed train-track-bridge model, the influence of wheel hollow wear on the vibration characteristics of the train-track-bridge system is investigated and presented in this section. Here, the new profile and the worn profile with travel distance of 192,000 km were taken as the input wheel profiles. Since the highest operational speed of high-speed trains in China is 350 km/h at present, the train speed in the simulations was also set to this value. The time domain sample of track irregularity obtained from the spectral transformation of low-disturbance track of German high-speed railway was applied.

Figures 17–19 show the wheel-rail forces of high-speed trains with new and worn profiles in time and frequency domains. Figure 17(a) shows that wheel wear has a certain effect on wheel-rail force. After severe wheel wear, it will increase the impact between wheel and rail, leading to a sharp increase in some peak values of wheel-rail force. Figure 17(b) shows that wheel wear has a greater impact on the lateral force of wheel and rail than the vertical force of wheel and rail. The amplitude of the lateral force of wheel and rail wearing wheel increases obviously. The maximum wheel-rail vertical force before and after wheel wear changed from 221.58 kN to 234.90 kN, which increased by 6.01%. The maximum wheel-rail lateral force before and after wheel wear increased from 9.84 kN to 14.38 kN, which increased by 46.1%.

In the frequency domain, wheel wear results in a slight increase in the high frequency of wheel-rail vertical force, as

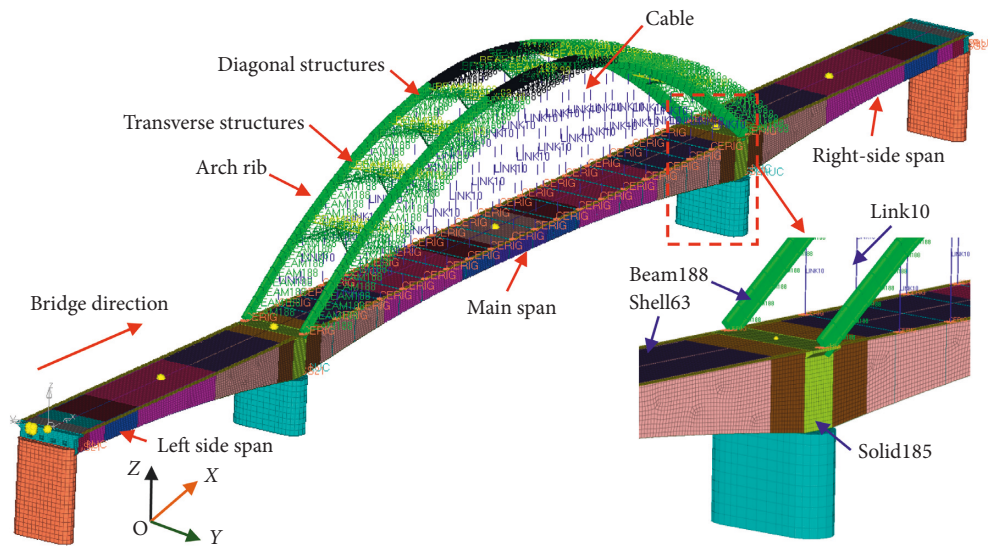

Figure 16: 3D FE model of the Chengjiang bridge.

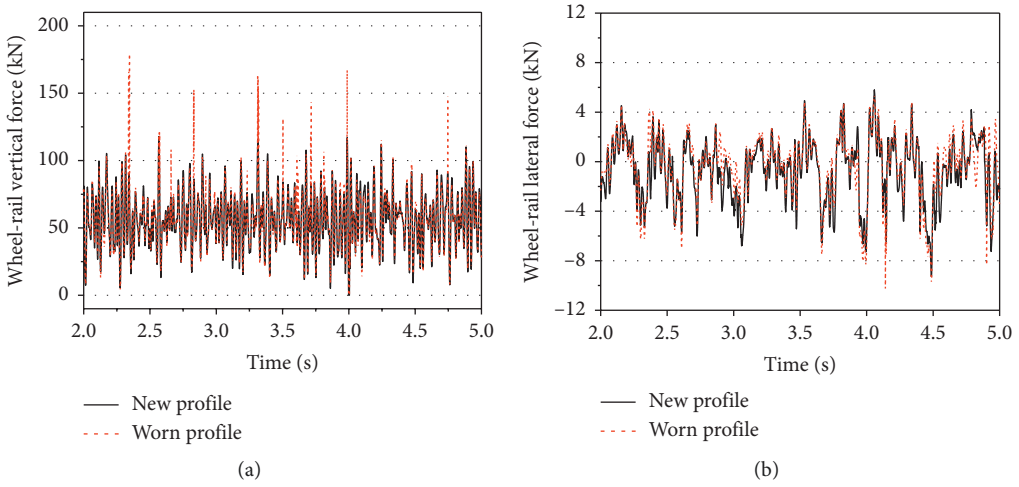

Figure 17: Wheel-rail force: (a) vertical; (b) lateral.

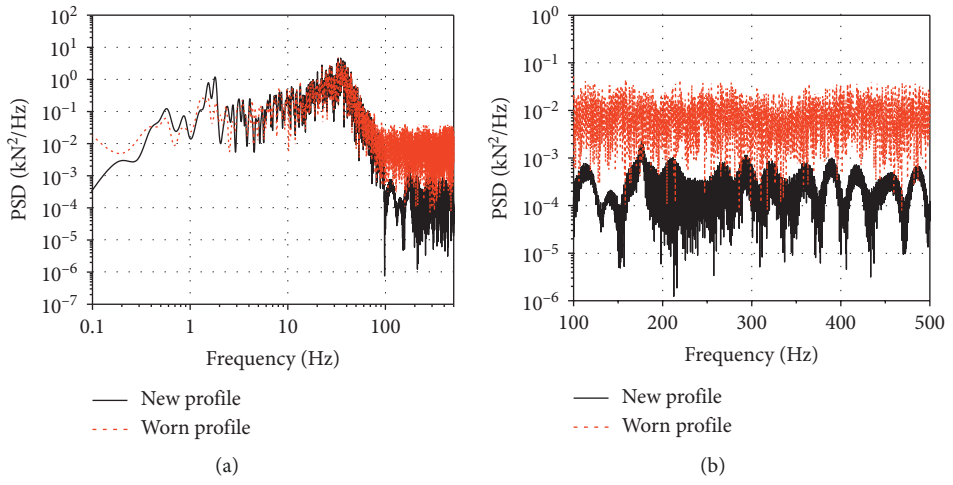

Figure 18: Power spectral density of vertical wheel-rail force: (a) overall; (b) enlarged diagram of 100~500 Hz.

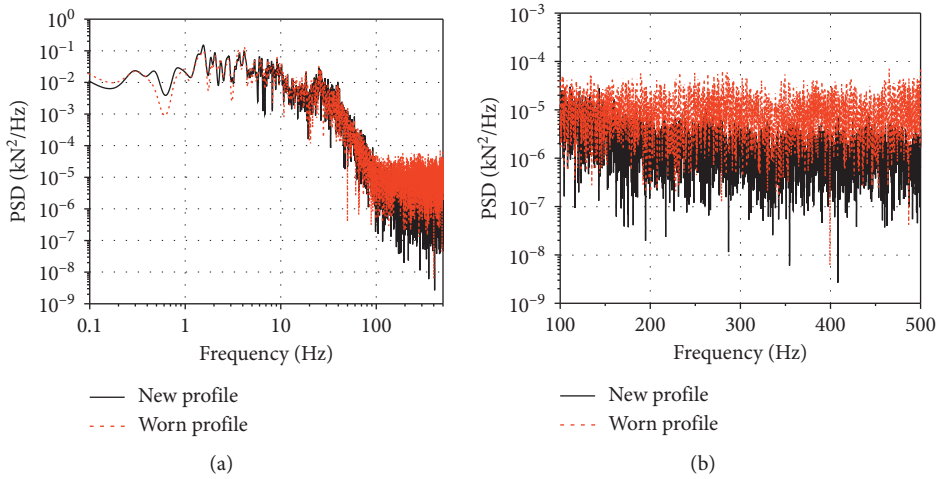

Figure 19: Power spectral density of lateral wheel-rail force: (a) overall; (b) enlarged diagram of 100~500 Hz.

shown in Figure 18. In the meanwhile, the increase in wheel-rail lateral force is mainly reflected in the middle and high frequencies from Figure 19. This shows that the wear of wheel material mainly affects the wheel-rail force in the middle and high frequencies domain, but has little effect on the low frequency wheel-rail force.

The dynamic responses of the bridge with initial (new) wheel profile and worn profile at 350 km/h speed are plotted in Figures 20–25. The vertical and lateral displacements of the midsection of the main span are shown in Figure 20. It reveals that wheel wear has little effect on the bridge displacement as the bridge displacement of the cases with worn and new profiles are basically the same. The vertical displacement curves are basically the same before and after the wheel profile changes, and the maximum values maintain at about 3.6 mm. The lateral displacement curves fluctuate slightly, but the amplitudes are quite small, the maximum values are stable around 0.11 mm.

Figures 21 and 22 depict the time histories of bridge vertical and lateral displacement of the left and right-side spans. Similar to the dynamic response of the main span, wheel wear has no obvious effect on the vertical displacement of the bridge, while small difference is found in the lateral displacements. The vertical displacement peak values of left and right span attain about 2 mm, and the lateral displacement peak values fluctuates around 0.06 mm.

Figures 23 and 24 display the time domain diagram of bridge vertical and lateral acceleration of the main span. It is not difficult to observe that the wheel wear has obvious effects on the vibration acceleration of the bridge. The maximum vertical accelerations of the cases with new and worn profiles were 0.0525 m/s^2 and 0.0643 m/s^2, respectively, which increased by 23.1%. The maximum values of lateral accelerations of the cases with new and worn profiles are 0.0138 m/s^2 and 0.0222 m/s^2, respectively, with an increase of 60.9%. The results show that the responses of bridge accelerations obtained with the models considering the wheel worn profiles are higher than those obtained by the models without considering wheel wear.

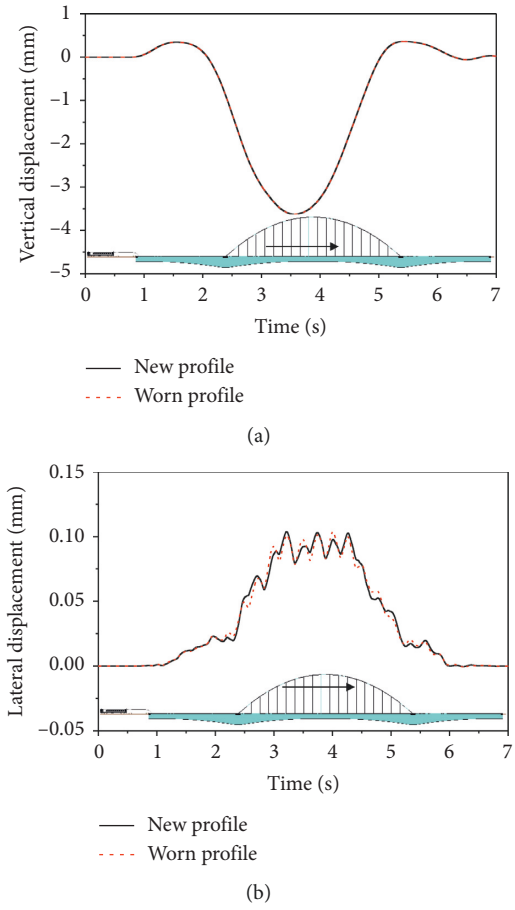

Figure 20: Time histories of displacement at the midsection of the main span (speed: $v = 350$ km/h): (a) vertical; (b) lateral.

Figure 25 shows the PSD diagram of the bridge vertical and lateral accelerations presented in Figures 23 and 24. For the vertical acceleration, the main frequencies appear around 0.53 Hz, 7.59 Hz, 22.9 Hz, and 26.9 Hz. But there is no obvious difference between the PSDs of the cases with new and worn profiles. This means that the wheel hollow

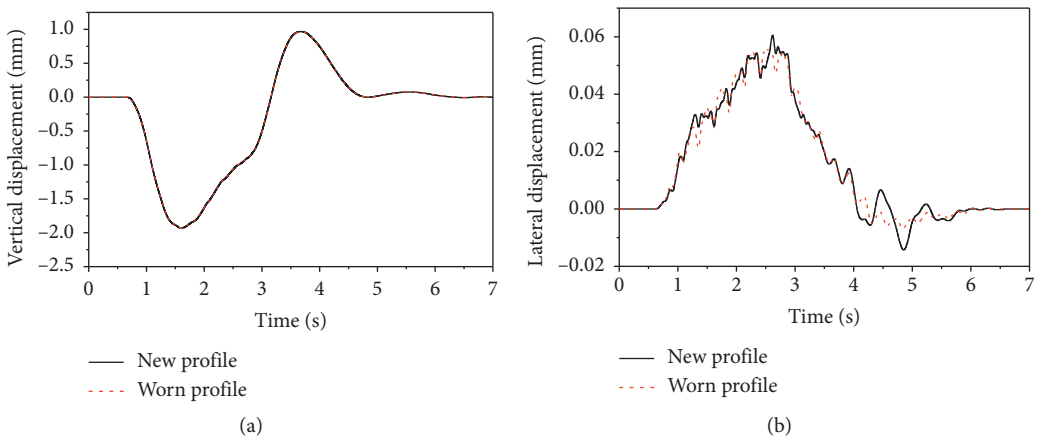

Figure 21: Time histories of displacement at the midsection of the left side span (speed: $v = 350$ km/h): (a) vertical; (b) lateral.

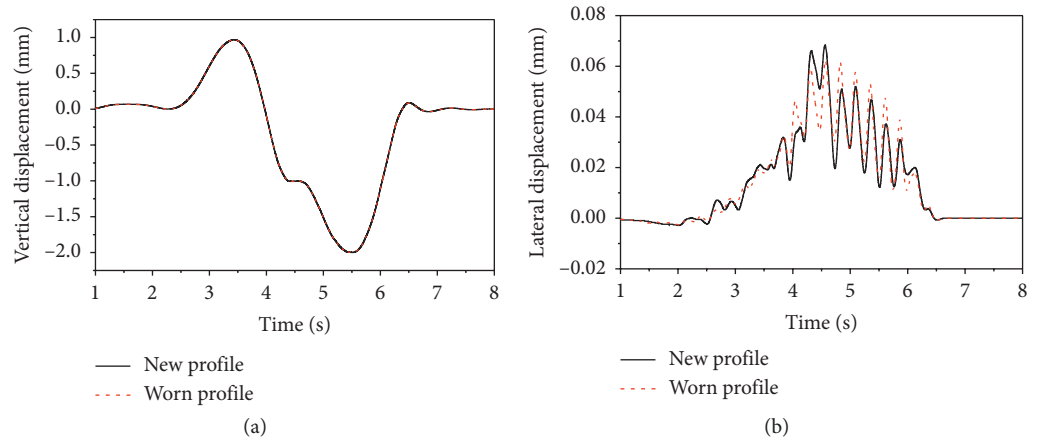

Figure 22: Time histories of displacement at the midsection of the right-side span (speed: $v = 350$ km/h): (a) vertical; (b) lateral.

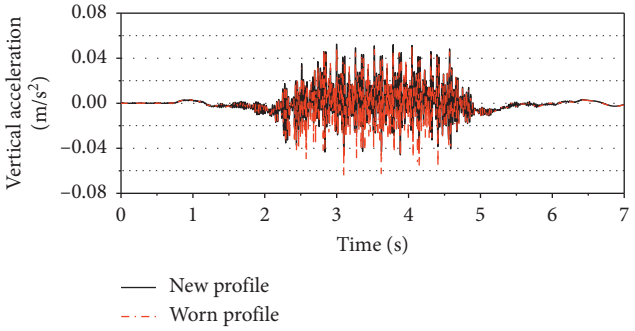

Figure 23: Time histories of vertical acceleration at the midsection of the main span (speed: $v = 350$ km/h).

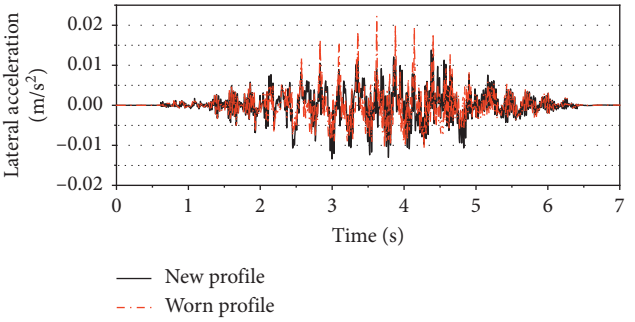

Figure 24: Time histories of lateral acceleration at the midsection of the main span (speed: $v = 350$ km/h).

wear has little effect on frequency domain curves of bridge vertical acceleration in the range of 0~30 Hz. For the lateral acceleration, the PSD changes obviously. After the wheel profile wear occurring, the peak frequency appearing at 1.53 Hz decreases significantly, while the peak frequency near 3.96 Hz increases obviously. It is noted that the peak frequencies of 1.53 Hz and 3.96 Hz are corresponded to the lateral modal shapes of the bridge girders. It indicates that the wheel hollow wear may cause the amplitude of bridge vibration acceleration to change or shift in frequency domain.

Figures 26 and Table 2 show the peak values of bridge accelerations and displacements of the main span, left-side span, and right-side span. The abscissa represents different operating mileage and corresponds to different worn wheel treads. From these results, the dynamic characteristics of the

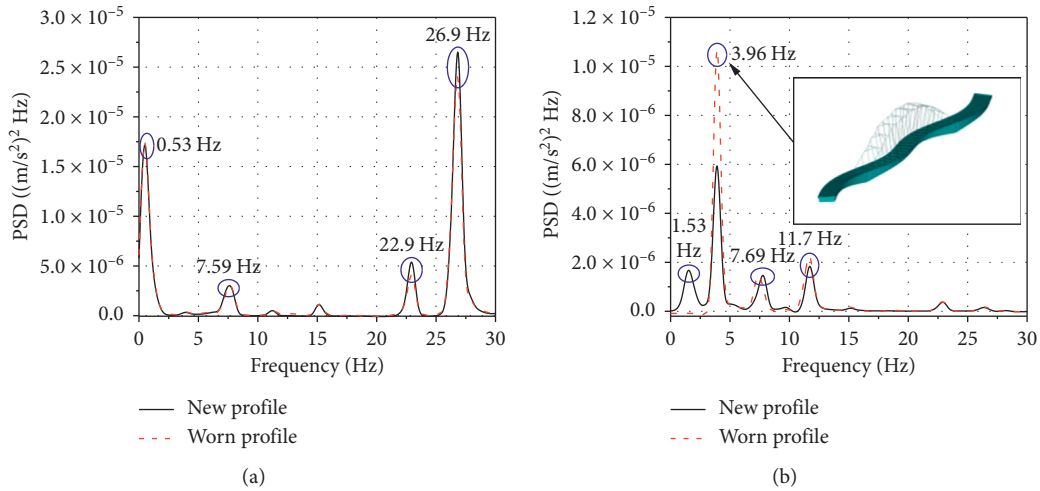

Figure 25: PSD analysis of bridge accelerations of the main span: (a) vertical; (b) lateral.

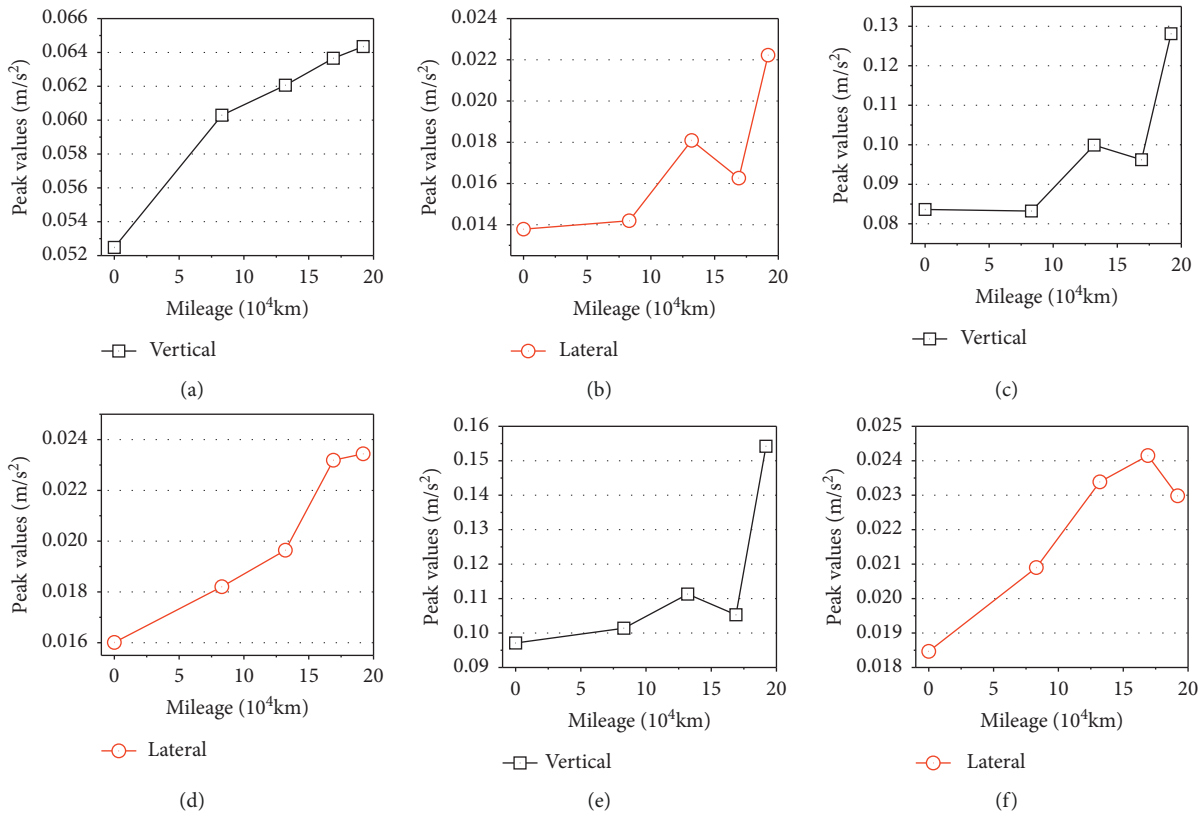

Figure 26: Peak values of bridge accelerations: (a) vertical acceleration of midspan; (b) lateral acceleration of midspan; (c) vertical acceleration of left-side span; (d) lateral acceleration of left-side span; (e) vertical acceleration of right-side span; (f) lateral acceleration of right-side span.

Table 2: The peak values of bridge displacement.

Operating mileage (×10⁴ km)	Midspan		Left-side span		Right-side span	
	Vertical	Lateral	Vertical	Lateral	Vertical	Lateral
0	3.6364	0.1022	1.9590	0.0606	1.9838	0.0672
8.3	3.6353	0.1037	1.9593	0.0563	1.9840	0.0608
13.2	3.6357	0.1028	1.9593	0.0558	1.9840	0.0606
16.9	3.6357	0.1011	1.9593	0.0558	1.9839	0.0603
19.2	3.6357	0.1037	1.9593	0.0558	1.9836	0.0625

bridge under different wheel worn profiles can be summarized as follows:

(1) The wheel hollow wear has little effect on the dynamic displacement of the long-span bridge. The reason should be that the bridge main girder has a large overall stiffness as it is made of high-strength concrete material, thus the displacement of the bridge is mainly related to the axle load and distribution characteristics of the train.

(2) The maximum bridge accelerations increase fast in lateral and vertical directions with the wheel wear depth increase. It shows that both vertical and lateral bridge accelerations are greatly affected by the change of wheel profile.

5. Conclusions

This paper reported a study of the high-speed train-track-bridge dynamic interactions considering the wheel-rail contact nonlinearity due to hollow worn wheel profiles. A nonlinear rigid-flexible coupled model of a high-speed train travelling on a long-span continuous girder bridge was established. The accuracy of the model is validated by comparing with the measured data. The vertical and lateral dynamic responses of the high-speed train-track-bridge system under new and worn wheel profiles were discussed.

The simulation results have shown that the wheel hollow wear of high-speed trains has a great influence on the geometric parameters of the wheel-rail contact, which can aggravate the wheel-rail interaction and finally deteriorates the train-track-bridge interactions. The wheel wear has little effect on the bridge dynamic displacement. However, the bridge vertical and lateral accelerations increase with the accumulation of the wheel hollow wear. It is suggested that the influence of worn wheel-rail profiles should be considered in the dynamic analysis of train-track-bridge interaction during the stage of bridge structure design and safety assessment.

Data Availability

The data used to support the findings of this study are available from the corresponding author upon request.

Conflicts of Interest

The authors declare that they have no conflicts of interest.

Acknowledgments

The authors would like to thank all the students involved in the on-track test from State Key Laboratory of Traction Power at Chengdu, China. This work was supported by the National Natural Science Foundation of China (grant nos. 51735012, 11790283, and 51805452), the Application Basic Research Project of Sichuan Province (grant no. 2019YJ0232), the Open Project of State Key Laboratory of Traction Power (grant no. 2018TPL_T09), and the Fundamental Research Funds for the Central Universities (grant no. 2682018CX67).

References

[1] W. M. Zhai, X. S. Jin, Z. F. Wen, and X. Zhao, "Wear problems of high-speed wheel/rail systems in china: observations, causes, and counter measures," in *Proceedings of the 11th International Conference on Contact Mechanics and Wear of Rail/wheel Systems*, Delft, Netherland, September 2018.

[2] X. He, T. Wu, Y. Zou, Y. F. Chen, H. Guo, and Z. Yu, "Recent developments of high-speed railway bridges in China," *Structure and Infrastructure Engineering*, vol. 13, no. 12, pp. 1584–1595, 2017.

[3] W. Zhai, Z. Han, Z. Chen, L. Ling, and S. Zhu, "Train–track–bridge dynamic interaction: a state-of-the-art review," *Vehicle System Dynamics*, vol. 57, no. 7, pp. 984–1027, 2019.

[4] W. M. Zhai, H. Xia, and C. B. Cai, "High-speed train–track–bridge dynamic interactions–part I: theoretical model and numerical simulation," *International Journal of Rail Transportation*, vol. 1, no. 1-2, pp. 3–24, 2013.

[5] W. M. Zhai, S. Wang, N. Zhang et al., "High-speed train–track–bridge dynamic interactions–part II: experimental validation and engineering application," *International Journal of Rail Transportation*, vol. 1, no. 1-2, pp. 25–41, 2013.

[6] N. Zhang and H. Xia, "Dynamic analysis of coupled vehicle–bridge system based on inter-system iteration method," *Computers & Structures*, vol. 114-115, pp. 26–34, 2013.

[7] V. N. Dinh, K. D. Kim, and P. Warnitchai, "Dynamic analysis of three-dimensional bridge–high-speed train interactions using a wheel–rail contact model," *Engineering Structures*, vol. 31, no. 12, pp. 3090–3106, 2009.

[8] Y. Li, X. Xu, Y. Zhou, C. Cai, and J. Qin, "An interactive method for the analysis of the simulation of vehicle–bridge coupling vibration using ANSYS and SIMPACK," *Proceedings of the Institution of Mechanical Engineers, Part F: Journal of Rail and Rapid Transit*, vol. 232, no. 3, pp. 663–679, 2018.

[9] L. R. T. Melo, T. N. Bittencourt, D. Ribeiro, and R. Calçada, "Dynamic response of a railway bridge to heavy axle-load trains considering vehicle–bridge interaction," *International Journal of Structural Stability and Dynamics*, vol. 18, no. 1, Article ID 1850010, pp. 1–27, 2018.

[10] P. Antolín, N. Zhang, J. M. Goicolea, H. Xia, M. Á. Astiz, and J. Oliva, "Consideration of nonlinear wheel–rail contact forces for dynamic vehicle–bridge interaction in high-speed railways," *Journal of Sound and Vibration*, vol. 332, no. 5, pp. 1231–1251, 2013.

[11] T. Arvidsson, A. Andersson, and R. Karoumi, "Train running safety on non-ballasted bridges," *International Journal of Rail Transportation*, vol. 7, no. 1, pp. 1–22, 2019.

[12] M. Dhanasekar, P. Prasad, J. Dorji, and T. Zahra, "Serviceability assessment of masonry arch bridges using digital image correlation," *Journal of Bridge Engineering*, vol. 24, no. 2, Article ID 04018120, pp. 1–16, 2019.

[13] Y. L. Li, S. F. Dong, Y. L. Bao, K. J. Chen, and S. Z. Qiang, "Impact coefficient analysis of long-span railway cable-stayed bridge based on coupled vehicle-bridge vibration," *Shock and Vibration*, vol. 2015, Article ID 641731, 9 pages, 2015.

[14] X. H. Zhang, Y. Shan, and X. W. Yang, "Effect of bridge-pier differential settlement on the dynamic response of a high-speed railway train-track-bridge system," *Mathematical Problems in Engineering*, vol. 2017, Article ID 8960628, 13 pages, 2017.

[15] Z.-P. Zeng, Y.-G. Zhao, W.-T. Xu, Z.-W. Yu, L.-K. Chen, and P. Lou, "Random vibration analysis of train–bridge under track irregularities and traveling seismic waves using train–slab track–bridge interaction model," *Journal of Sound and Vibration*, vol. 342, pp. 22–43, 2015.

[16] Z. P. Zeng, Z. W. Yu, Y. G. Yang, W.-T. Xu, L.-K. Chen, and P. Lou, "Numerical simulation of vertical random vibration of train-slab track-bridge interaction system by PEM," *Shock and Vibration*, vol. 2014, Article ID 304219, 21 pages, 2014.

[17] X. Kang, L. Jiang, Y. Bai, and C. C. Caprani, "Seismic damage evaluation of high-speed railway bridge components under different intensities of earthquake excitations," *Engineering Structures*, vol. 152, pp. 116–128, 2017.

[18] X. Yang, H. H. Wang, and X. L. Jin, "Numerical analysis of a train-bridge system subjected to earthquake and running safety evaluation of moving train," *Shock and Vibration*, vol. 2016, Article ID 9027054, 15 pages, 2016.

[19] Z. Chen, H. Fang, Z. Han, and S. Sun, "Influence of bridge-based designed TMD on running trains," *Journal of Vibration and Control*, vol. 25, no. 1, pp. 182–193, 2019.

[20] M. Luu, V. Zabel, and C. Könke, "An optimization method of multi-resonant response of high-speed train bridges using TMDs," *Finite Elements in Analysis and Design*, vol. 53, pp. 13–23, 2012.

[21] J. Lavado, A. Doménech, and M. D. Martínez-Rodrigo, "Dynamic performance of existing high-speed railway bridges under resonant conditions following a retrofit with fluid viscous dampers supported on clamped auxiliary beams," *Engineering Structures*, vol. 59, pp. 355–374, 2014.

[22] S. Rådeström, M. Ülker-Kaustell, A. Andersson, V. Tell, and R. Karoumi, "Application of fluid viscous dampers to mitigate vibrations of high-speed railway bridges," *International Journal of Rail Transportation*, vol. 5, no. 1, pp. 47–62, 2017.

[23] M. Luu, M. D. Martinez-Rodrigo, V. Zabel, and C. Könke, "Semi-active magnetorheological dampers for reducing response of high-speed railway bridges," *Control Engineering Practice*, vol. 32, pp. 147–160, 2014.

[24] L. Ling, M. Dhanasekar, and D. P. Thambiratnam, "Dynamic response of the train–track–bridge system subjected to derailment impacts," *Vehicle System Dynamics*, vol. 56, no. 4, pp. 638–657, 2018.

[25] L. Ling, M. Dhanasekar, K. Wang, W. Zhai, and B. Weston, "Collision derailments on bridges containing ballastless slab tracks," *Engineering Failure Analysis*, vol. 105, pp. 869–882, 2019.

[26] J. M. Rocha, A. A. Henriques, and R. Calçada, "Probabilistic assessment of the train running safety on a short-span high-speed railway bridge," *Structure and Infrastructure Engineering*, vol. 12, no. 1, pp. 78–92, 2016.

[27] Z.-W. Yu, J.-F. Mao, F.-Q. Guo, and W. Guo, "Non-stationary random vibration analysis of a 3D train–bridge system using the probability density evolution method," *Journal of Sound and Vibration*, vol. 366, pp. 173–189, 2016.

[28] K. Matsuoka, A. Collina, and M. Sogabe, "Dynamic simulation and critical assessment of a composite bridge in high-speed railway," *Procedia Engineering*, vol. 199, pp. 3027–3032, 2017.

[29] X. He, Y. Gai, and T. Wu, "Simulation of train–bridge interaction under wind loads: a rigid-flexible coupling approach," *International Journal of Rail Transportation*, vol. 6, no. 3, pp. 163–182, 2018.

[30] J. M. Olmos and M. Á. Astiz, "Non-linear vehicle-bridge-wind interaction model for running safety assessment of high-speed trains over a high-pier viaduct," *Journal of Sound and Vibration*, vol. 419, pp. 63–89, 2018.

[31] H. Qiao, H. Xia, and X. Du, "Dynamic analysis of an integrated train–bridge–foundation–soil system by the substructure method," *International Journal of Structural Stability and Dynamics*, vol. 18, no. 5, Article ID 1850069, pp. 1–25, 2018.

[32] O. Polach and D. Nicklisch, "Wheel/rail contact geometry parameters in regard to vehicle behaviour and their alteration with wear," *Wear*, vol. 366-367, pp. 200–208, 2016.

[33] H. Shi, J. Wang, P. Wu, C. Song, and W. Teng, "Field measurements of the evolution of wheel wear and vehicle dynamics for high-speed trains," *Vehicle System Dynamics*, vol. 56, no. 8, pp. 1187–1206, 2018.

[34] Z. S. Ren, "An investigation on wheel/rail impact dynamics with a three-dimensional flat model," *Vehicle System Dynamics*, vol. 57, no. 3, pp. 369–388, 2019.

[35] W. M. Zhai and H. Xia, *Train-Track-Bridge Dynamic Interaction: Theory and Engineering Application*, Science Press, Beijing, China, 2011.

[36] L. Ling, X.-B. Xiao, J.-Y. Xiong, L. Zhou, Z.-F. Wen, and X.-S. Jin, "A 3D model for coupling dynamics analysis of high-speed train/track system," *China's High-Speed Rail Technology*, vol. 15, no. 12, pp. 309–339, 2018.

[37] R. R. Craig and M. C. C. Bampton, "Coupling of substructures for dynamic analyses," *AIAA Journal*, vol. 6, no. 7, pp. 1313–1319, 1968.

[38] J.-G. Kim and P.-S. Lee, "An enhanced Craig–Bampton method," *International Journal for Numerical Methods in Engineering*, vol. 103, no. 2, pp. 79–93, 2015.

[39] J. Piotrowski and W. Kik, "A simplified model of wheel/rail contact mechanics for non-Hertzian problems and its application in rail vehicle dynamic simulations," *Vehicle System Dynamics*, vol. 46, no. 1-2, pp. 27–48, 2008.

[40] Y. Sun, Y. Guo, and W. Zhai, "Prediction of rail non-uniform wear—influence of track random irregularity," *Wear*, vol. 420-421, pp. 235–244, 2019.

[41] J. J. Kalker, "A fast algorithm for the simplified theory of rolling contact," *Vehicle System Dynamics*, vol. 11, no. 1, pp. 1–13, 1982.

[42] W. Zhai, P. Liu, J. Lin, and K. Wang, "Experimental investigation on vibration behaviour of a CRH train at speed of 350 km/h," *International Journal of Rail Transportation*, vol. 3, no. 1, pp. 1–16, 2015.

[43] TG/CL 127-2013, *Railway Electric Multiple Units Operation and Maintaining Regulation*, China Railway Corporation, Beijing, China, 2013.